Label-free oxygen-metabolic photoacoustic microscopy *in vivo*

Junjie Yao
Konstantin I. Maslov
Yu Zhang
Younan Xia
Lihong V. Wang

Label-free oxygen-metabolic photoacoustic microscopy *in vivo*

Junjie Yao, Konstantin I. Maslov, Yu Zhang, Younan Xia, and Lihong V. Wang
Washington University in St. Louis, Department of Biomedical Engineering, One Brookings Drive,
St. Louis, Missouri 63130

Abstract. Almost all diseases, especially cancer and diabetes, manifest abnormal oxygen metabolism. Accurately measuring the metabolic rate of oxygen (MRO_2) can be helpful for fundamental pathophysiological studies, and even early diagnosis and treatment of disease. Current techniques either lack high resolution or rely on exogenous contrast. Here, we propose label-free metabolic photoacoustic microscopy (mPAM) with small vessel resolution to noninvasively quantify MRO_2 *in vivo* in absolute units. mPAM is the unique modality for simultaneously imaging all five anatomical, chemical, and fluid-dynamic parameters required for such quantification: tissue volume, vessel cross-section, concentration of hemoglobin, oxygen saturation of hemoglobin, and blood flow speed. Hyperthermia, cryotherapy, melanoma, and glioblastoma were longitudinally imaged *in vivo*. Counterintuitively, increased MRO_2 does not necessarily cause hypoxia or increase oxygen extraction. In fact, early-stage cancer was found to be hyperoxic despite hypermetabolism. © *2011 Society of Photo-Optical Instrumentation Engineers (SPIE)*. [DOI: 10.1117/1.3594786]

1 Introduction

The energy demand of mammals is primarily met by aerobic metabolism, producing 88% of ATP molecules.[1] Therefore, the metabolic rate of oxygen (MRO_2) is an important indicator of tissue viability and functionality. It is known that nearly all cancers after the early stage are starved for oxygen (hypoxia) due to hypermetabolism and/or limited blood supply, regardless of their cellar origins.[2] In the presence of low oxygen pressure, highly malignant cancer cells survive and proliferate via glycolysis (anaerobic respiration, the Warburg effect). The presence of a large number of hypoxic regions within a tumor usually correlates with a poor prognosis.[1] This metabolic phenotype has become the basis for tumor imaging by positron emission tomography (PET) using radioactively labeled oxygen. Many other pathological and physiological functions are also closely related to alterations of oxygen metabolism: examples include Alzheimer's disease,[3] diabetes,[4] burns,[5] obstructive pulmonary disease,[6] congestive heart failure,[7] aging,[8] sleeping,[9] and physiologic challenges.[10] Therefore, an accurate measurement of MRO_2 has the potential to provide a powerful tool for diagnosis and therapy of cancer and other diseases as well as for metabolism-related pathophysiological studies.

Compared with other oxygenation indexes of tissue, i.e., oxygen saturation (sO_2) of hemoglobin and partial oxygen pressure (pO_2), MRO_2 is superior because it directly reflects the rate of oxygen consumption instead of the static oxygen concentration.[11] If the region of interest has well-defined feeding and draining vessels, we have[12]

$$MRO_2 = \varepsilon \times C_{Hb} \times (sO_{2in} \times A_{in} \times \bar{v}_{in} - sO_{2out} \times A_{out} \times \bar{v}_{out})/W. \tag{1}$$

Here, subscripts *in* and *out* denote feeding and draining vessels, respectively. ε is the oxygen binding capacity of hemoglobin and is usually taken as a constant (1.36 ml O_2/gram hemoglobin).[13] C_{Hb} is the total hemoglobin concentration (in grams of hemoglobin/ml blood). sO_2 is the average oxygen saturation (in %). A is the cross-sectional area (in mm^2). $\bar{v}$ is the average blood flow speed (in mm/s). W is the weight of the region of interest (in grams). While C_{Hb} can be estimated anywhere in the trunk vasculature, the other parameters must be locally measured.

Presently, three primary imaging modalities are used to quantify MRO_2.[12] Among them, PET is most widely used in clinical practice. However, the need for injection or inhalation of radioactively labeled exogenous tracers results in a complex procedure with exposure to ionizing radiation, limiting its usage.[14] Functional magnetic resonance imaging (fMRI) has also been intensively used for MRO_2 study, especially in the brain. fMRI is limited to qualitative evaluation of only temporal changes in MRO_2 and has difficulty in measuring both C_{Hb} and sO_2.[15] It also must switch between different imaging protocols to measure sO_2 and $\bar{v}$.[16,17] Moreover, both PET and fMRI are expensive. Diffuse optical tomography (DOT) is also capable of measuring MRO_2 and is relatively inexpensive, but it relies on an approximate theoretical model or other techniques (e.g., Doppler ultrasound and laser Doppler) to provide blood flow information.[18,19] Recently, DOT has been combined with diffuse correlation spectroscopy (DCS), which is capable of providing relative blood flow information.[20] Furthermore, due to their relatively poor spatial resolutions, PET,

---

Address all correspondence to: Lihong Wang, Washington University in St. Louis, Biomedical Engineering, One Brookings Drive, Campus Box 1097, St. Louis, Missouri 63130. Tel: 314 935 6152; Fax: 314 935 7448; E-mail: lhwang@biomed.wustl.edu.

fMRI, and DOT usually measure MRO_2 averaged over a large volume.[21]

Here, we overcome these limitations by developing label-free metabolic photoacoustic microscopy (mPAM) that ultrasonically measures optical contrast through the photoacoustic (PA) effect. For the first time, we demonstrated that all five anatomic, chemical, and fluid-dynamic parameters for MRO_2 quantification can be obtained in absolute units by mPAM alone *in vivo*. To validate mPAM, first we studied the MRO_2 responses to hyperthermia and cryotherapy, two common therapeutic techniques. Furthermore, mPAM was used to longitudinally image melanoma and glioblastoma, demonstrating its capability of early cancer detection.

2 Materials and Methods

2.1 Ethical Review of Procedures

All experimental animal procedures were carried out in conformity with the laboratory animal protocol approved by the Animal Studies Committee at Washington University in St. Louis.

2.2 Experimental Animals

The ears of adult, four- to five-week-old nude mice (Hsd: Athymic Nude-Foxl[NU], Harlan Co.; body weight: ~20 g) were used for all *in vivo* experiments. During data acquisition, the animal was held steady with a dental/hard palate fixture and kept still by using a breathing anesthesia system (E-Z Anesthesia, Euthanex). After the experiment, the animal naturally recovered and was returned to its cage. For tumor study, after monitoring, the animal was sacrificed by an intraperitoneal administration of pentobarbital at a dosage of 120 mg/kg.

2.3 Metabolic Photoacoustic Microscopy

Metabolic photoacoustic microscopy [Fig. 1(a)] is based on newly developed photoacoustic microscopy, which has shown a robust capability to noninvasively image microvasculature using endogenous contrast with high spatial resolution (lateral: ~5 μm; axial: ~15 μm).[22] Briefly speaking, a tunable dye laser (CBR-D, Sirah) pumped by a Nd:YLF laser (INNOSAB, Edgewave, 523 nm) serves as the light source. The laser pulse is reshaped by a 25-μm diameter pinhole and focused onto the surface of the mouse ear by a microscope objective lens (Olympus 4×, NA = 0.1) with a pulse energy of ~100 nJ. Ultrasonic detection is achieved through a spherically focused ultrasonic transducer (V2012-BC, Panametrics-NDT), which is confocally placed with the objective. The detected PA signal is then amplified, digitized, and saved. A volumetric image is generated by recording the time-resolved PA signal (A-line) at each horizontal location of the two-dimensional raster scan. The motion controller provides the trigger signals for laser firing, data acquisition, and motor scanning.
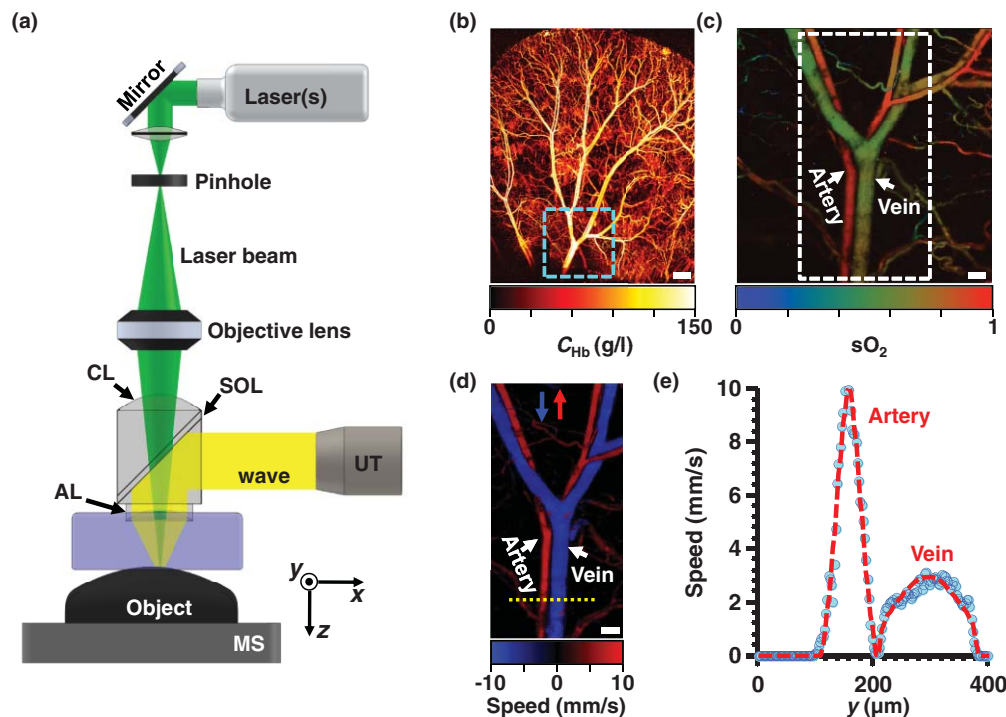

Fig. 1 Label-free quantification of MRO_2 *in vivo*. (a) Schematic of mPAM system. Nanosecond laser pulses pass through a pinhole and are focused on the animal's skin surface by an objective. The resultant PA signal is detected by a focused ultrasonic transducer, which is confocally placed with the objective. A transverse resolution of 5 μm and an axial resolution of 15 μm are achieved, with a penetration depth greater than 700 μm. CL: correction lens; AL: acoustic lens; SQL: silicone oil layer; UT: ultrasonic transducer; WT: water tank; MS: motorized scanner. (b) mPAM image of the total concentration of hemoglobin (C_{Hb}). Scale bar: 500 μm. (c) mPAM image of the sO_2 of hemoglobin in the area indicated by the dashed box in (b). Scale bar: 125 μm. (d) mPAM image of blood flow in the area indicated by the dashed box in (c). Red arrow: positive scanning direction; blue arrow: negative scanning direction. Positive velocity: upward flow. Scale bar: 125 μm. (e) Profile of blood flow speed across the dashed line in (d). (Color online only.)

All of the parameters for MRO_2 quantification in Eq. (1) can be simultaneously obtained by mPAM. Specifically, anatomic parameters W and A are quantified from the structural mPAM image;[23] functional parameters C_{Hb} and sO_2 are measured by laser excitation at two wavelengths;[23,24] fluid-dynamic parameter $\bar{v}$ is estimated on the basis of photoacoustic Doppler bandwidth broadening of the PA signal induced by circulating red blood cells.[25,26] The structural image acquisition time is ∼25 min for a 4 mm × 4 mm region (∼1 Hz frame rate) using a single wavelength; the oxygenation image acquisition time is ∼20 min for a 1 mm × 1 mm region using two wavelengths (∼0.3 Hz frame rate); the flow speed acquisition time is ∼5 min for a 0.5 mm cross-sectional line using a single wavelength.

2.4 Hyperthermia Experimental Protocol

In the hyperthermia study, the animal's temperature was regulated by adjusting the water temperature in the heating pad placed underneath its abdomen. The water was circulated by a water-bath system (ISOTEMP 9100, Fisher Scientific). A cotton layer between the heating pad and the animal skin buffered and homogenized the temperature change and thus protected the animal from burns. The room temperature was kept at 23 °C. The animal's skin temperature (SKT) was monitored on the dorsal pelvis by an attached electronic thermometer (Radio Shack, Cat. No. 63-854). Before the experiment, the SKT was adjusted to 31 °C, which was used as the baseline. The experiment was divided into three periods. The animal was first monitored at baseline temperature for ∼40 min (the resting period), then heated for ∼30 min by increasing the heading pad to 50 °C (the heating period), and last allowed to cool to baseline for ∼100 min (the recovery period). The hemodynamic parameters were simultaneously measured on the principal artery-vein pair (AVP) using mPAM. Each measurement took ∼6 min and the whole experiment lasted for ∼3 h.

2.5 Tumor Cell Culture

B16 mouse melanoma cells were obtained from the Tissue Culture and Support Center at the Washington University School of Medicine. The cells were maintained in Dulbecco's modified Eagle medium (DMEM, Invitrogen, Carlsbad, California) supplemented with 10% fetal bovine serum (FBS) and 1% P/S. U87 MG human brain glioblastoma cells (HTB-14) were obtained from American Type Cell Culture (ATCC). The cells were maintained in Eagle's Minimum Essential Medium (EMEM, Invitrogen) supplemented with 10% heat-inactivated FBS (ATCC) and 1% penicillin-streptavidin (P/S, Invitrogen). The cultures were performed at 37 °C and 5% CO_2 and the cells were passaged weekly.

2.6 Inoculation of Tumor Cells

In the tumor study, 0.01 ml of suspension containing ∼0.5 million B16 melanoma cells or U87 human glioblastoma cells was inoculated into the top skin layer in the left ear of a nude mouse, using a 0.3 ml syringe with a 29-gauge needle. The injection was usually located near the second order branch of the principal AVP above the cartilage. The tumor was allowed to grow and monitored for one to three weeks. A control measurement was performed before the tumor cell injection (day zero).

2.7 Hemodynamics Measured by Metabolic Photoacoustic Microscopy

The hemodynamic parameters were monitored using mPAM on the principal AVP, which included vessel diameter, total hemoglobin concentration, oxygen saturation, blood flow direction, and flow speed.

1. Vessel diameter. The vessel diameter was measured along a cross-section perpendicular to the vessel centerline. A threshold of two times the noise level was empirically set to separate the background and vessel. The transverse dimension of the vessel cross section was taken as the vessel diameter D, in case the excitation light could not penetrate the whole vessel in the axial direction. Then the vessel cross-section area was calculated as $A = \pi (D/4)^2$. Five adjacent cross sections were measured and the mean value of the principal vein was used for MRO_2 calculation.

2. Total hemoglobin concentration. Since oxy- and deoxyhemoglobin have the same absorption coefficient at 584 nm, the PA signal amplitude is proportional to the total hemoglobin concentration regardless of the oxygen saturation level.[27] On the basis of a previous study,[28] the total hemoglobin concentration was set to be 146.0 g/l at baseline temperature (the hyperthermia study) and on day zero (the tumor and cryotherapy studies). The sequential data sets were accordingly calibrated. The averaged PA signal amplitude along the centerline of the principal vein was used for calculation.

3. Oxygen saturation. The sO_2 was measured using laser excitations at 584 and 590 nm, respectively.[24] The relative change in molar extinction coefficient is ∼58.4% for oxy- and 17.5% for deoxy-hemoglobin, respectively. Because the vessels studied here were big enough (> 50 μm) and the laser pulse energy was low (∼100 nJ), the difference of penetration depth will not affect the results much. The PA signal at each wavelength was normalized with the laser pulse energy, as monitored by a wavelength-calibrated photodiode. The averaged sO_2 along the vessel centerline was used for the MRO_2 calculation. The PA image acquired at 584 nm was used as a mask on the sO_2 image to remove the background noise.

4. Blood flow direction. The blood flow direction was measured on the basis of photoacoustic Doppler bandwidth broadening with bidirectional motor scanning at 584 nm.[25] The laser repetition rate was 3 KHz and the scanning step size was 0.625 μm. We used 64 sequential A-lines to calculate the bandwidth broadening. If the blood flow had a positive projection along the positive scanning direction, we defined it as a positive flow and vice versa. The mPAM image acquired at 584 nm was used as a mask on the flow image to remove the background noise.

5. Blood flow speed. To better estimate the flow speed, *M*-mode imaging at 584 nm was used to measure the bandwidth broadening across the vessel. The laser repetition rate was 3 KHz and 3200 A-lines were acquired at each position. The flow speed at each position was calculated on the basis of the Doppler bandwidth broadening. The average amplitude of the PA signal at each position was used as a mask on the speed profile to remove the background noise. The mean flow speed of the principal vein was used for MRO_2 calculation.

2.8 Melanoma Volume Estimation using Metabolic Photoacoustic Microscopy

After data acquisition, the PA signal amplitude acquired at each optical wavelength was extracted through the Hilbert transformation. The tumor region was then separated from the surrounding blood vessels according to the mPAM image acquired at 605 nm, where melanin has much stronger absorption than blood. A threshold of 20% of the maximum signal amplitude was set to segment the tumor. Since it was challenging to penetrate through the whole tumor due to the high absorption of melanin, a 3D envelope of the tumor region was obtained from the surface signal instead. The volume of the tumor was then cal-

culated by integrating the corresponding voxels enclosed by the envelope. All of the image processing was conducted using the MATLAB Image Processing Toolbox (R2008a, MathWorks).

2.9 Fitting for the Profile of Blood Flow Speed

A theoretical model was used to fit the profile of the blood flow speed across the vessel,[29]

$$v(x) = v_{\max} \times \left[1 - \left(\frac{x - x_0}{R}\right)^n\right]. \qquad (2)$$

Here, x is the transverse location, x_0 is the vessel center, R is the vessel radius, $v_{\max}$ is the flow speed at the vessel center, and n is the power index that characterizes the flow profile (e.g., $n = 2$ for laminar flow). While x_0 and R can be directly measured from the mPAM images of the vessel structure, $v_{\max}$ and n are the unknown parameters to fit for.

2.10 Statistical Analysis

Quantitative data was expressed as mean $\pm$ s.e.m. The statistical test is a paired Student's *t*-test (two-tailed with unequal variance), compared with the baseline levels (hyperthermia and cryotherapy studies) or day zero (tumor studies). We considered a *p*-value less than 0.05 to be statistically significant.
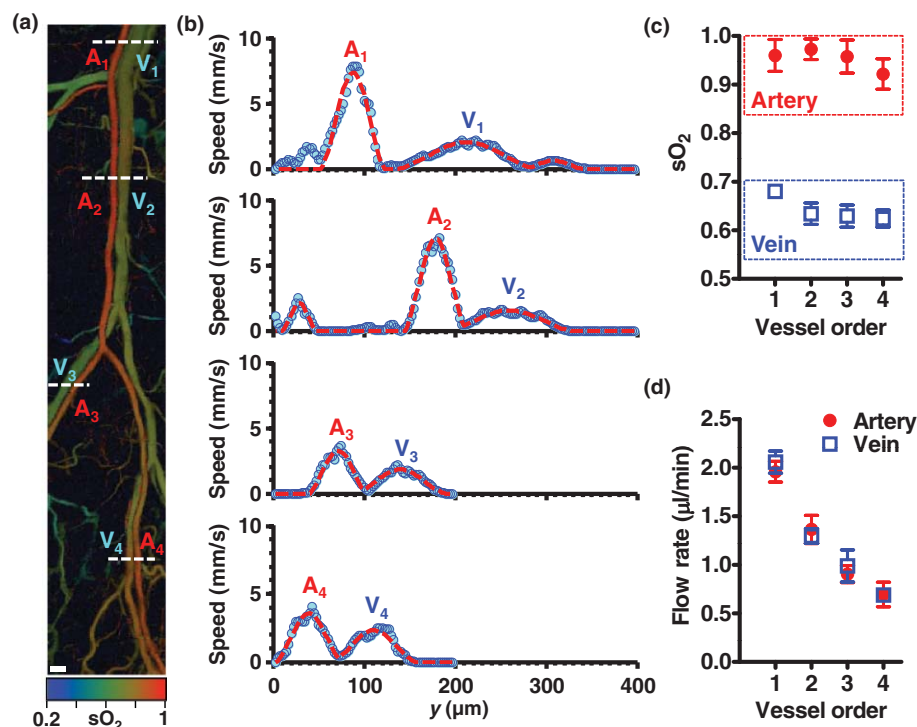

Fig. 2 mPAM measurements of sO_2 and blood flow on four orders of artery-vein pairs in the mouse ear. (a) sO_2 mapping from two measurements at 584 and 590 nm. Four different orders of artery-vein pairs are labeled. Scale bar: 125 μm. (b) Profiles of blood flow speed across vessels of different orders measured along the dashed lines in (a) on the basis of PA Doppler bandwidth broadening at 584 nm. Generally, the flow speed decreases from the proximal order to the distal order. However, it also depends on the vessel diameter as a result of the conservation of total flow. Solid circles: experimental data; red curves: fit. (c) Mean sO_2 versus the vessel order, quantified along the centerline of each vessel. The sO_2 values in both the arteries and veins slightly change with the vessel order, especially at distal branches. This is probably due to oxygen diffusion between the arteries and veins, and the inhomogeneous MRO_2. (d) Blood flow rate (in μl/min) versus the vessel order, quantified from the flow speed profiles and vessel diameters. Blood flow in both arteries and veins decreases from the proximal order to the distal order and is conserved between the artery and vein of the same order. The blood fed by the artery is mostly drained by the corresponding vein of the same order. V: vein; A: artery. (Color online only.)

3 Results

3.1 Metabolic Rate of Oxygen Quantification under Normothermia

The nude mouse ear is a good model for validating mPAM because of its similarity to human skin and lack of motion artifacts.[30–32] Each artery-vein pair (AVP) feeds a well-defined region while one pair at the base of the ear feeds the entire ear (Fig. 2).[33,34] Consequently, the MRO_2 based on each AVP approximates the MRO_2 of its supplied region.

As an example, we measured the MRO_2 of a mouse ear under normothermia. The animal's temperature was regulated with a heating pad placed under its abdomen (skin temperature: 31 °C) and a volumetric image was acquired using mPAM at 584 nm by scanning a 10 mm × 8 mm area containing the principal AVP [Fig. 1(b)]. Because 584 nm is an isosbestic wavelength for hemoglobin, this image maps the concentration of total hemoglobin regardless of the oxygen saturation level. In addition, it measures the diameters of the principal AVP (artery: ~65 μm; vein: ~116 μm). Two PAM images acquired at 584 and 590 nm were then used to calculate sO_2 [Fig. 1(c)].[23] The vessels with high sO_2 values (>90%) are classified as arteries, whereas the vessels with low sO_2 values (60 to 80%) are veins. The blood flow velocity was measured at 584 nm using bi-directional scanning with a laser repetition rate of 3 KHz and a motor step size of 0.625 μm [Fig. 1(d)]. The profile of flow speed across the principal AVP is shown in Fig. 1(e). The artery

and the vein have a mean flow speed of 5.5 and 1.8 mm/s, respectively, and the speed profiles are both approximately parabolic.[29] The weight of the mouse ear was computed by its volume in the 3D PA image, where the average specific weight was assumed to be 1.0 g/ml.[35] From these measurements, the MRO_2 of the mouse ear was estimated to be 0.23 ml/100 g/min, which agrees with the data previously measured in humans.[2]

3.2 Change in Metabolic Rate of Oxygen Induced by Systemic Hyperthermia

Hyperthermia has been clinically used for cancer treatment.[36] To measure MRO_2 during hyperthermia, the mouse's skin temperature was elevated to 42 °C [Fig. 3(a)]. Hemodynamics were monitored on the principal of AVP. The vessel diameter started increasing at the beginning of the heating period [Fig. 3(b)] and reached a maximum by the end of the heating period. The total hemoglobin concentration of the principal AVP kept increasing after the heating started and plateaued when the temperature returned to the baseline [Fig. 3(c)]. This cumulative effect was due to a decrease in blood plasma volume resulting from water loss during hyperthermia.[37] From the change in sO_2 [Fig. 3(d)], we found that the oxygen extraction fraction (OEF, defined as $(sO_{2in} - sO_{2out})/sO_{2in}$ and represents the fraction of O_2 molecules that cross the capillary wall) decreased by 12% over the heating period and eventually recovered to 99% of the resting level [Fig. 3(f)]. The measurements of flow speed in the
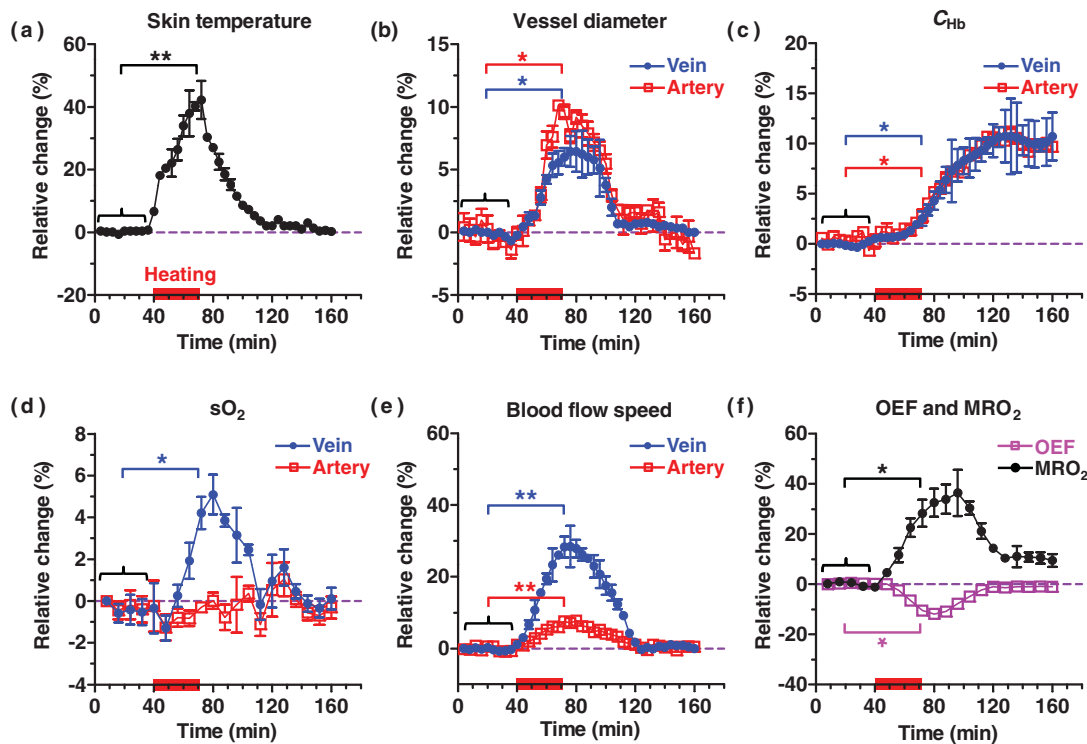

Fig. 3 mPAM measurement of hemodynamic responses to a hyperthermic challenge (red bars). Relative changes of (a) the skin temperature, (b) vessel diameter, (c) total hemoglobin concentration, (d) sO_2, (e) blood flow speed, and (f) OEF and MRO_2. Statistics: paired Student's *t*-test. * $p < 0.05$, ** $p < 0.01$, $n = 3$. Data are presented as means ± s.e.m. The baseline values are (a) temperature: 31.0 ± 0.4 °C, (b) vessel diameters: 92.5 ± 10.5 μm (vein) and 47.5 ± 8.5 μm (vein), (c) C_{Hb}: 146.3 ± 18.1 g/l (vein) and 148.5 ± 14.0 g/l (artery), (d) sO_2: 0.70 ± 0.08 (vein) and 0.94 ± 0.04 (artery), (e) flow speeds: 1.3 ± 0.4 mm/s (vein) and 5.1 ± 0.8 mm/s (artery), and (f) 0.26 ± 0.13 (OEF) and 0.30 ± 0.09 ml/100 g/min (MRO_2). (Color online only.)
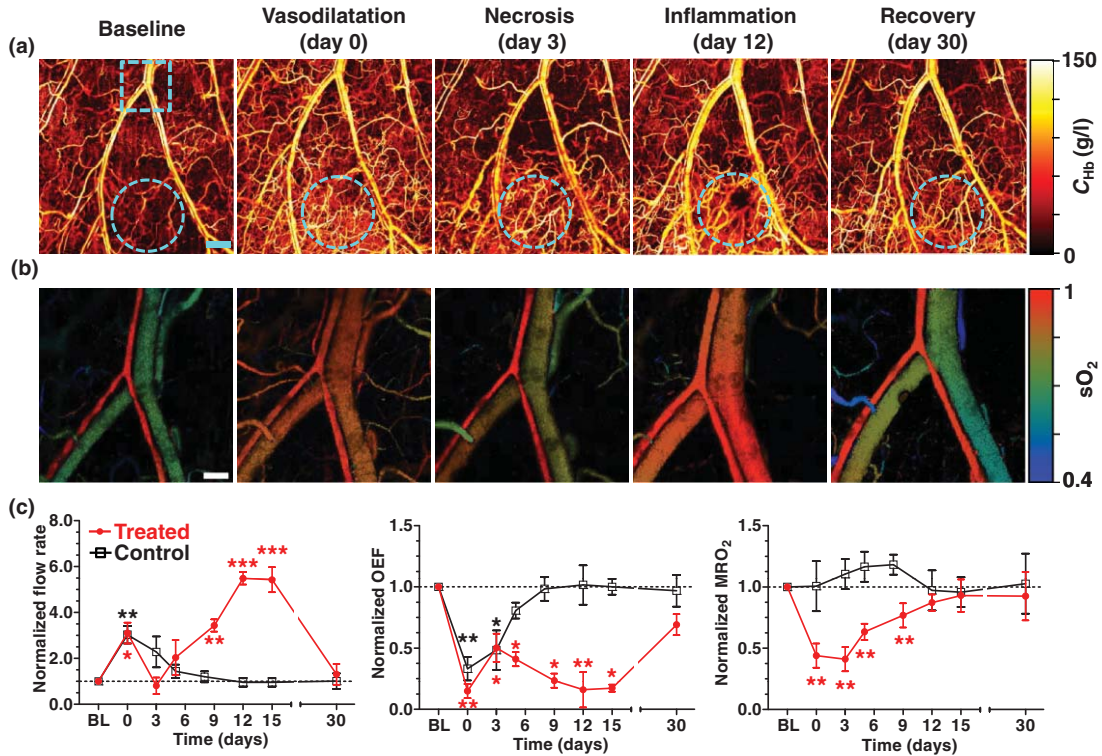
Fig. 4 mPAM monitoring of hemodynamic responses after cryotherapy. (a) mPAM vasculature images acquired in different phases before and after the application of liquid nitrogen. The treated area is indicated by cyan dashed circles. Scale bar: 500 μm. (b) mPAM images of sO_2 in the artery-vein pair [cyan dashed box in (a)] that supports the treated area. Scale bar: 125 μm. (c) mPAM quantification of blood flow rate, OEF and MRO_2 within 30 days after the treatment. A neighboring area close to the treated region was monitored as a control. Statistics: paired Student's *t*-test. * $p < 0.05$, ** $p < 0.01$, *** $p < 0.001$, $n = 4$. Data are presented as means $\pm$ s.e.m. Baseline flow rates: 0.72 ± 0.12 μl/min (treated) and 0.44 ± 0.15 μl/min (control); baseline OEF: 0.35 ± 0.04 (treated) and 0.31 ± 0.05 (control); baseline MRO_2: 0.30 ± 0.06 ml/100 g/min (treated) and 0.25 ± 0.07 ml/100 g/min (control). BL: baseline. (Color online only.)
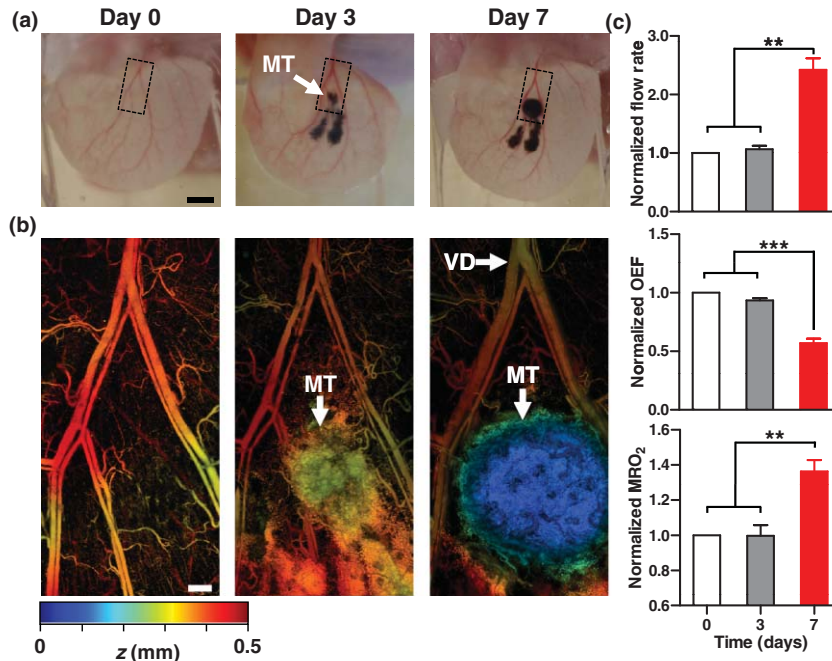

Fig. 5 mPAM detection of early-stage melanoma by measuring MRO_2. (a) White-light photographs of a representative mouse ear before (day 0), three and seven days after the xenotransplantation of B16 melanoma tumor cells. Scale bar: 1 mm. (b) mPAM images of the tumor region [dashed boxes in (a)] at 584 nm. *z* is coded by colors: blue (superficial) to red (deep). Scale bar: 125 μm. (c) mPAM quantification of blood flow rate, OEF and MRO_2 before (day zero), three and seven days after the tumor xenotransplantation, normalized by the values of day zero (flow rate: 1.77 ± 0.50 μl/min; OEF: 0.31 ± 0.04; MRO_2: 0.38 ± 0.03 ml/100 g/min). Statistics: paired Student's *t*-test. ** $p < 0.01$, *** $p < 0.001$, $n = 5$. Data are presented as means $\pm$ s.e.m. MT: melanoma tumor; VD: vasodilatation. (Color online only.)
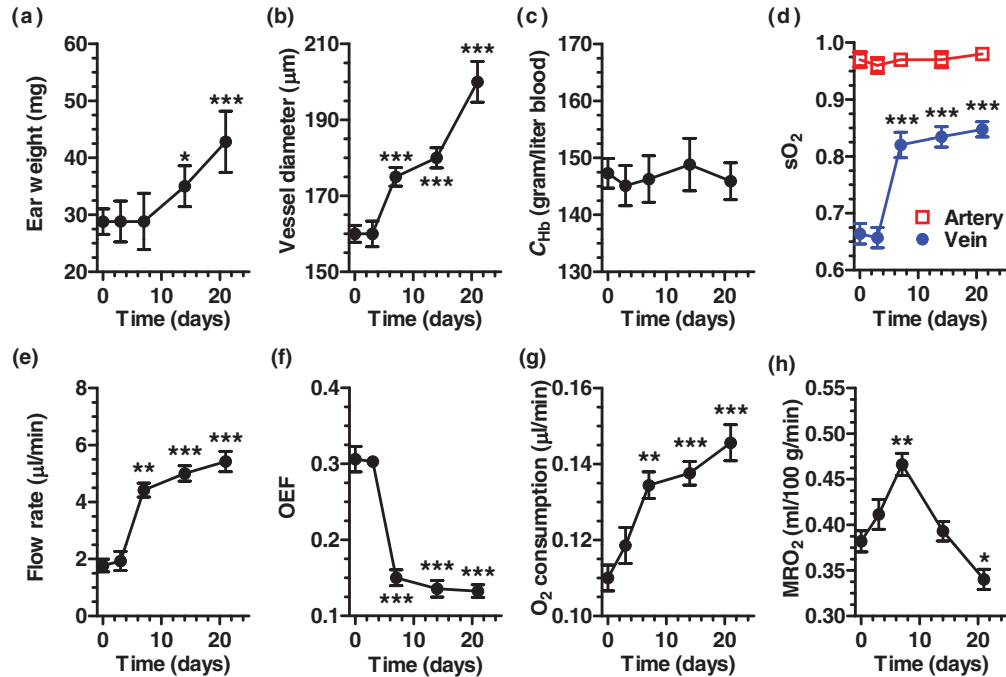
Fig. 6 mPAM characterization of melanoma progression. mPAM measurements in absolute units of (a) ear weight, (b) vessel diameter, (c) total hemoglobin concentration, (d) sO_2 of hemoglobin, (e) volumetric blood flow rate, (f) OEF, (g) rate of O_2 consumption in $\mu l/min$, and (h) MRO_2 in ml/100 g/min up to 21 days after tumor inoculation. Statistics: paired Student's *t*-test. * $p < 0.05$, ** $p < 0.01$, *** $p < 0.001$, $n = 3$. Data are presented as means $\pm$ s.e.m.

arteries during the heating were saturated because of the limited maximum measurable speed of the system [Fig. 3(e)]. From the measurements on the principal veins, we found the volumetric flow rate of blood entering the ear increased by 45%. Increased cardiac output and redistribution of blood to the skin are two major reasons for vessel dilation and faster blood flow, which help accelerate heat exchange with the environment.[36, 38] Note that the vessel diameter, sO_2, and blood flow speed reach the peaks approximately simultaneously.

The MRO_2 of the mouse ear, as computed from the hemodynamic changes, increased by 28% over the heating period [Fig. 3(f)], which indicated elevated oxygen metabolism during hyperthermia in response to an increased rate of enzymatic reactions.[39] This finding can potentially elucidate another possible mechanism for cell death induced by hyperthermia. When normal cells encounter such an increased metabolism, increased blood flow provides more nutrients. By contrast, cancer cells could be damaged owing to inadequate blood circulation. Therefore, hyperthermia may kill cancer cells by both protein denaturation and cell starvation due to heating.

3.3 Change in Metabolic Rate of Oxygen Induced by Local Cryotherapy

Cryotherapy has been found effective for treating cancer and other diseases by forming ice crystals inside cells.[40, 41] Here, we applied liquid nitrogen to the mouse ear surface for 10 s via a 1-mm diameter cryo-probe and monitored the hemodynamics of the treated area [Figs. 4(a) and 4(b)]. An untreated neighboring area of the same ear was also monitored as a control. Right after the treatment, a global reflective vasodilatation was observed on both the treated and control areas, which was accompanied by an increase in blood flow and a decrease in OEF. While the MRO_2
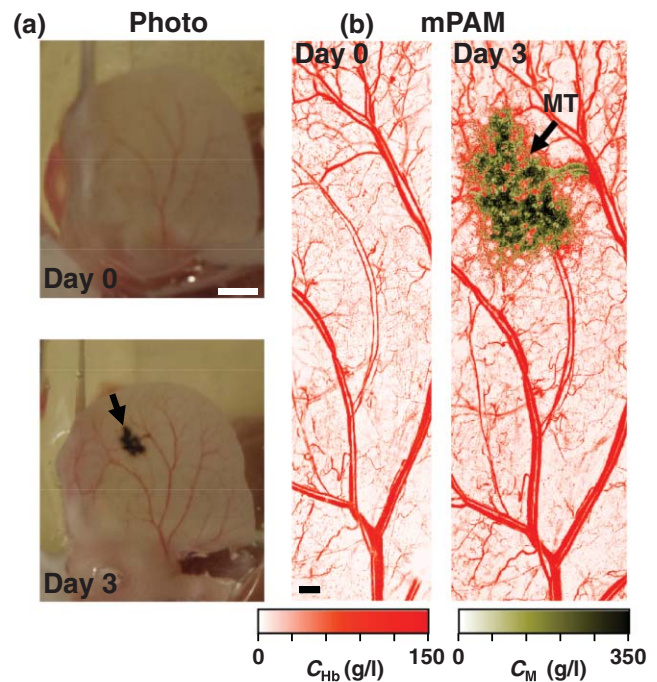

Fig. 7 mPAM differentiation of blood vessels and melanoma. (a) White-light photographs of a representative mouse ear before and three days after the xenotransplantation of B16 melanoma cells. Scale bar: 1 mm. (b) Composite mPAM images of blood vessels (in red) and melanoma (in brown). The two are differentiated by using dual-wavelength excitation at 584 and 605 nm. C_{Hb}: total hemoglobin concentration. C_M: melanin concentration. Scale bar: 250 μm. MT: melanoma tumor. (Color online only.)
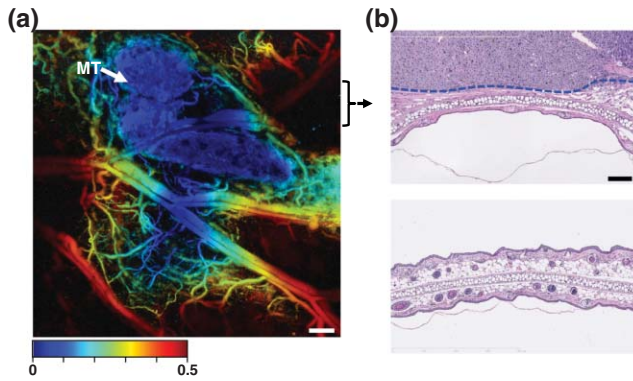
(a)

(b)

Fig. 8 Histological validation of melanoma detection. (a) mPAM image of a mouse ear bearing a B16 melanoma tumor acquired on day seven. z is coded by colors: blue (superficial) to red (deep). Scale bar: 300 μm. (b) Images of H&E stained tissue slices cut approximately across the tumor area (top) and nontumor area (bottom). Scale bar: 150 μm. MT: melanoma tumor. (Color online only.)

of the control area remained statistically unchanged, the MRO_2 of the treated area decreased by 56% due to the induced cell death. Therefore, mPAM can be used to evaluate the efficacy of cryotherapy. Within one month after the treatment, while all of the parameters of the control area monotonically recovered to the baseline, the physiological progress of the treated area occurred in phases [Fig. 4(c)]. Within three days following the reflective vasodilatation, blood flow and OEF trended toward the baseline, but MRO_2 remained at a low level due to cell necrosis. Starting from day five, inflammation was clearly observed, which was

triggered by the immune system and was helpful for both dead cell clearance and new cell growth. Although the OEF continued to decrease due to the increased flow speed,[11] the MRO_2 of the treated area eventually returned to the baseline, reflecting improved tissue viability. One month later, the inflammation nearly ended and all of the parameters had recovered almost to the baseline.

This study shows that each physiological phase after cryotherapy imparts its signature on the local MRO_2. The common belief is that inflammation triggered by the immune response further helps kill tumor cells.[42] However, our results show that the increased blood flow rate during inflammation may assist the survival of residual tumor cells by providing more nutrients and thus recovering the MRO_2 level.

3.4 Early Cancer Detection by Measuring Tumor-induced Change in Metabolic Rate of Oxygen

The third demonstration of mPAM is early cancer detection by measuring MRO_2. The hemodynamics of the mouse ear were longitudinally monitored after the injection of B16 melanoma cells [Fig. 5(a)]. On day 7, vessel dilation appeared around the tumor site as shown in Figs. 5(b) and 6(b). The volumetric blood flow rate increased by 1.5 fold [Figs. 5(c) and 6(e)]. These changes are important to ensure the supply of oxygen and nutrients to the rapidly growing tumor and to provide routes for tumor cell metastasis.[43] The overall OEF of the tumor region decreased by 43% [Figs. 5(c) and 6(f)] due to the increased blood flow.[11] The vasculature and melanoma were differentiated according to
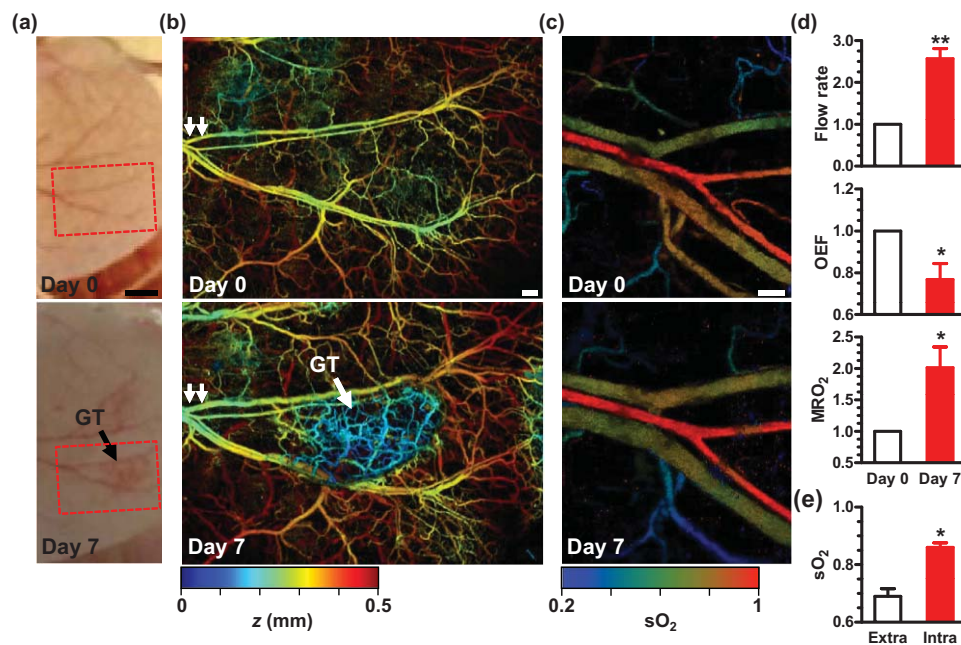

Fig. 9 mPAM detection of early-stage glioblastoma by measuring MRO_2. (a) White-light photographs of a representative mouse ear before (day zero) and seven days after the xenotransplantation of U87 glioblastoma tumor cells. Scale bar: 2 mm. (b) mPAM images of microvasculature in the tumor region [dashed boxes in (a)] at 584 nm. z is coded by colors: blue (superficial) to red (deep). Scale bar: 250 μm. (c) mPAM images of sO_2 in the artery-vein pair [double arrows in (b)] that supports the tumor region acquired on day zero and day seven. Scale bar: 100 μm. (d) mPAM quantification of volumetric blood flow rate, OEF and MRO_2 seven days after the tumor xenotransplantation, normalized by the values of day zero (flow rate: 1.03 $\pm$ 0.41 μl/min; OEF: 0.27 $\pm$ 0.03; MRO_2: 0.31 $\pm$ 0.09 ml/100 g/min). (e) Comparison of the averaged sO_2 values in the intra- and extra-tumoral vasculatures. Statistics: paired Student's t-test. * $p < 0.05$, ** $p < 0.01$, $n = 5$. Data are presented as means $\pm$ s.e.m. GT: glioblastoma tumor. (Color online only.)
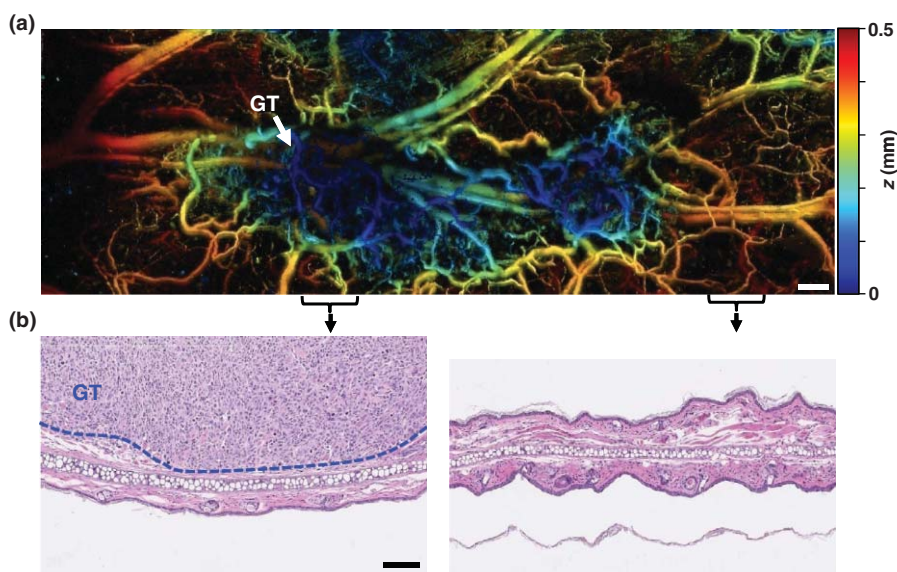
Fig. 10 Histological validation of glioblastoma detection. (a) mPAM image of a mouse ear bearing a U87 glioblastoma tumor acquired on day seven. z is coded by colors: blue (superficial) to red (deep). Scale bar: 250 μm. (b) Images of H&E stained tissue slices cut approximately across the tumor (left) and nontumor areas (right). Scale bar: 150 μm. GT: glioblastoma tumor. (Color online only.)

their different absorption spectra using dual-wavelength excitation at 584 and 605 nm, and thus the tumor volume could be estimated (Fig. 7). The hypermetabolism of melanoma was reflected by a 36% increase in MRO_2 [Fig. 5(c)], which proves the early cancer detection capability of mPAM. The presence of the melanoma was confirmed by histology (Fig. 8). However, the melanoma was hyperoxic instead of hypoxic in the early stage [Fig. 6(d)]. On day 14, MRO_2 dropped to the baseline level and continued to decrease [Fig. 6(h)], even though the total oxygen consumption rate steadily increased [Fig. 6(g)]. There are two possible reasons for the final decline in MRO_2. On one hand, a tumor changes to anaerobic respiration instead of aerobic respiration when it grows too quickly to get sufficient oxygen;[2] on the other hand, when the tumor grows too large, the tumor core dies due to a decrease in available nutrients (necrosis). The necrotic tumor core does not consume oxygen but increases tumor weight [Fig. 6(a)], which decreases the MRO_2.[44]

Besides melanoma, we also studied U87 human glioblastoma [Fig. 9(a)], which is more transparent; thus, its intratumoral vasculature can be better visualized. On day seven, angiogenesis was observed within the tumor region [Fig. 9(b)], and the sO_2 of the draining vein was found to be increased, indirectly indicating early-stage tumor hyperoxia [Fig. 9(c)]. The presence of the glioblastoma was confirmed by histology (Fig. 10). While the increase in blood supply for the glioblastoma was comparable with that for the melanoma, the OEF showed a decrease by 24% instead of 43% [Fig. 9(d)]. We observed a 100% increase in MRO_2 instead of 36% for the melanoma, which indicated a stronger hypermetabolism at the early stage of glioblastoma. However, characteristic of early-stage cancer,[45] such hypermetabolism did not lead to tumor hypoxia. In fact, the sO_2 in the intratumoral vasculature was even higher than that of the surrounding normal tissue, directly indicating early-stage tumor hyperoxia [Fig. 9(e)]. The increase in sO_2 actually caused the decrease in OEF in the tumor. This observation suggests that a hypoxia-based diagnosis may not apply to early-stage cancer.[46]

4 Conclusions and Discussion

The observations presented here demonstrate the power of mPAM as the only noninvasive label-free imaging modality that can measure all of the parameters required for the quantification of MRO_2 in absolute units. Whereas MRO_2 is the ultimate measure of oxygen metabolism, OEF and sO_2 can be misleading partial measures. Unlike as is commonly believed, a decrease in OEF or an increase in sO_2 does not necessarily indicate a decrease in MRO_2. Strikingly, we found early-stage cancer to be hyperoxic instead of hypoxic despite the hypermetabolism.

mPAM can noninvasively measure anatomical, functional, and fluid-dynamic information at the resolution of small vessels, making it possible for MRO_2 quantification in microenvironments. MRO_2-based early cancer detection and evaluation of its treatment are highly desirable. mPAM also has various other prospective applications related to MRO_2. First, its high spatial resolution is essential for micro-hemodynamic studies, such as monitoring of local hemorrhage caused by mini-strokes. Second, its high sensitivity is critical for studies concerning small metabolic changes, such as the monitoring of neurovascular coupling in response to physiological challenges. Third, its potentially real-time imaging through fast optical scanning or ultrasonic-array detection is important for studies involving short transition times between physiological states, e.g., monitoring of epileptic seizures. Finally, its high spatial scalability enables us to correlate microscopic and macroscopic studies (e.g., monitoring of local neuron firing and overall brain activity) based on the same contrast. Overall, mPAM has strong potential for the study of metabolism in cancer and other metabolic diseases.

References

1. T. N. Seyfried and L. M. Shelton, "Cancer as a metabolic disease," *Nutr. Metab.* **7**(7), 1–22 (2010).
2. P. Vaupel, F. Kallinowski, and P. Okunieff, "Blood-flow, oxygen and nutrient supply, and metabolic microenvironment of human-tumors – a review," *Cancer Res.* **49**(23), 6449–6465 (1989).
3. X. Zhang and W. D. Le, "Pathological role of hypoxia in Alzheimer's disease," *Exp. Neurol.* **223**(2), 299–303 (2010).
4. K. Cheng, K. Ho, R. Stokes, C. Scott, S. M. Lau, W. J. Hawthorne, P. J. O'Connell, T. Loudovaris, T. W. Kay, R. N. Kulkarni, T. Okada, X. H. L. Wang, S. H. Yim, Y. Shah, S. T. Grey, A. V. Biankin, J. G. Kench, D. R. Laybutt, F. J. Gonzalez, C. R. Kahn, and J. E. Gunton, "Hypoxia-inducible factor-1 alpha regulates beta cell function in mouse and human islets," *J. Clin. Invest.* **120**(6), 2171–2183 (2010).
5. T. Tadros, D. L. Traber, and D. N. Herndon, "Hepatic blood flow and oxygen consumption after burn and sepsis," *J. Trauma: Inj., Infect., Crit. Care* **49**(1), 101–108 (2000).
6. M. Donahoe, R. M. Rogers, D. O. Wilson, and B. E. Pennock, "Oxygen-consumption of the respiratory muscles in normal and in malnourished patients with chronic obstructive pulmonary-disease," *Am. Rev. Respir. Dis.* **140**(2), 385–391 (1989).
7. R. M. Bersin, C. Wolfe, M. Kwasman, D. Lau, C. Klinski, K. Tanaka, P. Khorrami, G. N. Henderson, T. Demarco, and K. Chatterjee, "Improved hemodynamic function and mechanical efficiency in congestive-heart-failure with sodium dichloroacetate," *J. Am. Coll. Cardiol.* **23**(7), 1617–1624 (1994).
8. G. Marchal, P. Rioux, M. C. Petittaboue, G. Sette, J. M. Travere, C. Lepoec, P. Courtheoux, J. M. Derlon, and J. C. Baron, "Regional cerebral oxygen-consumption, blood-flow, and blood-volume in healthy-human aging," *Arch. Neurol.* **49**(10), 1013–1020 (1992).
9. P. Maquet, "Sleep function(s) and cerebral metabolism," *Behav. Brain Res.* **69**(1–2), 75–83 (1995).
10. A. de la Zerda, Z. A. Liu, S. Bodapati, R. Teed, S. Vaithilingam, B. T. Khuri-Yakub, X. Y. Chen, H. J. Dai, and S. S. Gambhir, "Ultrahigh sensitivity carbon nanotube agents for photoacoustic molecular imaging in living mice," *Nano Lett.* **10**(6), 2168–2172 (2010).
11. R. B. Buxton and L. R. Frank, "A model for the coupling between cerebral blood flow and oxygen metabolism during neural stimulation," *J. Cereb. Blood Flow Metab.* **17**(1), 64–72 (1997).
12. L. V. Wang, "Prospects of photoacoustic tomography," *Med. Phys.* **35**(12), 5758–5767 (2008).
13. A. C. Guyton and J. E. Hall, *Textbook of Medical Physiology*, (Elsevier Saunders, Elsevier Science distributor, Edinburgh, Oxford (2006).
14. R. S. J. Frackowiak, G. L. Lenzi, T. Jones, and J. D. Heather, "Quantitative measurement of regional cerebral blood-flow and oxygen-metabolism in man using O-15 and positron emission tomography – theory, procedure, and normal values," *J. Comput. Assist. Tomogr.* **4**(6), 727–736 (1980).
15. R. D. Hoge, J. Atkinson, B. Gill, G. R. Crelier, S. Marrett, and G. B. Pike, "Investigation of BOLD signal dependence on cerebral blood flow and oxygen consumption: the deoxyhemoglobin dilution model," *Magn. Reson. Med.* **42**(5), 849–863 (1999).
16. F. Xu, Y. L. Ge, and H. Z. Lu, "Noninvasive quantification of whole-brain cerebral metabolic rate of oxygen (CMRO2) by MRI," *Magn. Reson. Med.* **62**(1), 141–148 (2009).
17. V. Jain, M. C. Langham, and F. W. Wehrli, "MRI estimation of global brain oxygen consumption rate," *J. Cereb. Blood Flow Metab.* **30**(9), 1598–1607 (2010).
18. D. W. Brown, J. Hadway, and T. Y. Lee, "Near-infrared spectroscopy measurement of oxygen extraction fraction and cerebral metabolic rate of oxygen in newborn piglets," *Pediatr. Res.* **54**(6), 861–867 (2003).
19. D. A. Boas, G. Strangman, J. P. Culver, R. D. Hoge, G. Jasdzewski, R. A. Poldrack, B. R. Rosen, and J. B. Mandeville, "Can the cerebral metabolic rate of oxygen be estimated with near-infrared spectroscopy?," *Phys. Med. Biol.* **48**(15), 2405–2418 (2003).
20. C. Zhou, R. Choe, N. Shah, T. Durduran, G. Yu, A. Durkin, D. Hsiang, R. Mehta, J. Butler, A. Cerussi, B. J. Tromberg and A. G. Yodh, "Diffuse optical monitoring of blood flow and oxygenation in human breast cancer during early stages of neoadjuvant chemotherapy," *J. Biomed. Opt.* **12**(5), 051903 (2007).
21. S. Hu and L. V. Wang, "Photoacoustic imaging and characterization of the microvasculature," *J. Biomed. Opt.* **15**(1), 011101 (2010).
22. K. Maslov, H. F. Zhang, S. Hu, and L. V. Wang, "Optical-resolution photoacoustic microscopy for in vivo imaging of single capillaries," *Opt. Lett.* **33**(9), 929–931 (2008).
23. S. Hu, K. Maslov, V. Tsytsarev, and L. V. Wang, "Functional transcranial brain imaging by optical-resolution photoacoustic microscopy," *J. Biomed. Opt.* **14**(4), 040503 (2009).
24. H. F. Zhang, K. Maslov, G. Stoica, and L. H. V. Wang, "Functional photoacoustic microscopy for high-resolution and noninvasive in vivo imaging," *Nat. Biotechnol.* **24**(7), 848–851 (2006).
25. J. Yao, K. I. Maslov, Y. Shi, L. A. Taber, and L. V. Wang, "In vivo photoacoustic imaging of transverse blood flow by using Doppler broadening of bandwidth," *Opt. Lett.* **35**(9), 1419–1421 (2010).
26. J. J. Yao and L. H. V. Wang, "Transverse flow imaging based on photoacoustic Doppler bandwidth broadening," *J. Biomed. Opt.* **15**(2), 021304 (2010).
27. M. Sivaramakrishnan, K. Maslov, H. F. Zhang, G. Stoica, and L. V. Wang, "Limitations of quantitative photoacoustic measurements of blood oxygenation in small vessels," *Phys. Med. Biol.* **52**(5), 1349–1361 (2007).
28. E. S. Russell, E. F. Neufeld, and C. T. Higgins, "Comparison of normal blood picture of young adults from 18 inbred strains of mice," *Proc. Soc. Exp. Biol. Med.* **78**(3), 761–766 (1951).
29. R. S. C. Cobbold, *Foundations of Biomedical Ultrasound*, (Oxford University, New York, 2007).
30. E. J. Rebar, Y. Huang, R. Hickey, A. K. Nath, D. Meoli, S. Nath, B. L. Chen, L. Xu, Y. X. Liang, A. C. Jamieson, L. Zhang, S. K. Spratt, C. C. Case, A. Wolffe, and F. J. Giordano, "Induction of angiogenesis in a mouse model using engineered transcription factors," *Nat. Med.* **8**(12), 1427–1432 (2002).
31. R. K. Jain, K. Schlenger, M. Hockel, and F. Yuan, "Quantitative angiogenesis assays: progress and problems," *Nat. Med.* **3**(11), 1203–1208 (1997).
32. T. Tammela, G. Zarkada, E. Wallgard, A. Murtomaki, S. Suchting, M. Wirzenius, M. Waltari, M. Hellstrom, T. Schomber, R. Peltonen, C. Freitas, A. Duarte, H. Isoniemi, P. Laakkonen, G. Christofori, S. Yla-Herttuala, M. Shibuya, B. Pytowski, A. Eichmann, C. Betsholtz, and K. Alitalo, "Blocking VEGFR-3 suppresses angiogenic sprouting and vascular network formation," *Nature* **454**(7204), 656–U668 (2008).
33. E. Eriksson, J. V. Boykin, and R. N. Pittman, "Method for in vivo microscopy of the cutaneous microcirculation of the hairless mouse ear," *Microvasc. Res.* **19**(3), 374–379 (1980).
34. J. H. Barker, F. Hammersen, I. Bondar, E. Uhl, T. J. Galla, M. D. Menger, and K. Messmer, "The hairless mouse ear for in vivo studies of skin microcirculation," *Plast. Reconstr. Surg.* **83**(6), 948–959 (1989).
35. M. Rins, I. Diez, A. C. Calpena, and R. Obach, "Skin density in the hairless rat. Evidence of regional differences," *Eur. J. Drug Metab. Pharmacokinet* **3**, 456–457 (1991).
36. T. E. Dudar and R. K. Jain, "Differential response of normal, and tumor microcirculation to hyperthermia," *Cancer Res.* **44**(2), 605–612 (1984).
37. S. G. Rhind, G. A. Gannon, P. N. Shek, I. K. M. Brenner, Y. Severs, J. Zamecnik, A. Buguet, V. M. Natale, R. J. Shephard, and M. W. Radomski, "Contribution of exertional hyperthermia to sympathoadrenal-mediated lymphocyte subset redistribution," *J. Appl. Physiol.* **87**(3), 1178–1185 (1999).
38. N. Charkoudian, "Skin blood flow in adult human thermoregulation: how it works, when it does not, and why," *Mayo Clin. Proc.* **78**(5), 603–612 (2003).
39. R. T. Pettigre, J. M. Galt, C. M. Ludgate, D. B. Horn, and A. N. Smith, "Circulatory and biochemical effects of whole-body hyperthermia," *Brit. J. Surg.* **61**(9), 727–730 (1974).

40. P. Perrotte, J. Tran, E. J. McGuire, and L. L. Pisters, "Effect of prior therapy on survival after salvage cryotherapy for recurrent prostate cancer," *Prostate Cancer Prostatic Dis.* **2**(S3), S25–S25 (1999).
41. P. J. A. Holt, "Cryotherapy for skin-cancer – results over a 5-year period using liquid-nitrogen spray cryosurgery," *Br. J. Dermatol.* **119**(2), 231–240 (1988).
42. J. J. A. Joosten, G. N. P. van Muijen, T. Wobbes, and T. J. M. Ruers, "In vivo destruction of tumor tissue by cryoablation can induce inhibition of secondary tumor growth: an experimental study," *Cryobiology* **42**(1), 49–58 (2001).
43. G. H. Mahabeleshwar and T. V. Byzova, "Angiogenesis in melanoma," *Semin. Oncol.* **34**(6), 555–565 (2007).
44. R. M. Sutherland, "Cell and environment interactions in tumor microregions – the multicell spheroid model," *Science* **240**(4849), 177–184 (1988).
45. A. L. Harris, "Hypoxia – A key regulatory factor in tumour growth," *Nat. Rev. Cancer* **2**(1), 38–47 (2002).
46. J. Pouyssegur, F. Dayan, and N. M. Mazure, "Hypoxia signalling in cancer and approaches to enforce tumour regression," *Nature* **441**(7092), 437–443 (2006).